Ionization and fragmentation of C_{60} by highly charged, high-energy xenon ions

S. Cheng,* H. G. Berry,† R. W. Dunford, H. Esbensen, D. S. Gemmell, E. P. Kanter, and T. LeBrun
Physics Division, Argonne National Laboratory, Argonne, Illinois 60439

W. Bauer
National Superconducting Cyclotron Laboratory, Michigan State University, East Lansing, Michigan 48824
(Received 11 March 1996; revised manuscript received 19 June 1996)

C_{60} vapor was bombarded by $^{136}Xe^{35+}$ and $^{136}Xe^{18+}$ ions in the energy range 420–625 MeV to study the various ionization and fragmentation processes that occur. Since the center-of-mass energies used in this work exceeded those of previous studies by several orders of magnitude, new excitation and dissociation modes were expected and indeed found. Positive ions were extracted from the interaction region and their times of flight were measured both singly and in coincidence with other ionic fragments. A wide range of stable charge states and cluster sizes from monatomic carbon up to C_{60} was observed. Even-numbered carbon fragments dominated the heavier mass range but both even and odd carbon numbers occurred at lower masses. Evidence was found for three qualitatively different ionization and fragmentation channels suggesting different ranges of collision impact parameters: ionization of the parent C_{60} molecule, loss of even numbers of carbon atoms, and ''multifragmentation'' into many small fragments. This latter mode included the production of singly charged C_n^+ fragments with all values of n being observed from $n=1$ up to at least $n=19$. We interpret our results in terms of a theoretical model that indicates that the total interaction cross section contains comparable contributions from (a) excitation of the giant dipole plasmon resonance, and (b) large-energy-transfer processes that lead to multiple fragmentation of the molecule. The distribution of fragment cluster masses for $n \lesssim 20$ is reproduced by a ''percolation theory'' description analogous to that used to describe multifragmentation of nuclei by high-energy protons. [S1050-2947(96)06310-X]

PACS number(s): 36.40.Qv, 34.90.+q

I. INTRODUCTION

The discovery [1] of the highly stable and symmetric quasispherical molecule C_{60} and related fullerenes has led to intense studies on a wide variety of the properties of this new form of carbon. Research on these open cagelike structures received a big boost when methods were developed [2,3] to produce them in macroscopic quantities.

Among many approaches to the study of fullerenes, the use of atomic collision techniques offers a powerful tool for investigating their structures and their dynamics. Such studies fall naturally into two categories: (a) those that use an accelerated ion beam to bombard a fullerene target, and (b) those that employ an accelerated beam of fullerene ions. A difference between these two approaches lies in the fact that ionized fullerene projectiles can have a high and usually ill-determined internal energy, a complication that does not arise in the case of a fullerene target where the internal energies are thermal and thus relatively small. In both categories of study, the center-of-mass (CM) collision energies have been generally less than a few keV per nucleon and indeed mostly in the range below a few eV per nucleon. This has been a consequence either of the use of relatively low energy beams (for the most part <10 keV) to bombard fullerenes or of the large CM recoil motion involved in bombardments with fullerene beams. To our knowledge, the highest energy beams of C_{60}^+ thus far obtained are those that have been accelerated up to 36 MeV in a tandem Van der Graaf accelerator [4].

The collision studies conducted to date have displayed a number of interesting characteristics. For example, at CM energies in the approximate range 10–100 eV collisions between C_{60}^+ and the rare gases [5,6] result in bimodal fragment distributions peaking around C_{50}^+ and C_{15}^+, and this has been postulated [6] as indicating the collision-induced fission of C_{60}^+. The heavier fragments range from C_{32}^+ to C_{58}^+ and all contain even numbers of carbon atoms, consistent with observations in many other fullerene fragmentation experiments (see, for example, Refs. [7–14]). In the lower-mass range, C_n^+ fragments are found with augmented intensities at $n=11$, 15, 19, and 23. These numbers with their periodicity of four are identical with the ''magic numbers'' seen in the fragment distributions in laser vaporization of graphite [8] and in the high-fluence photodissociation of fullerenes [9]. In these low-energy collisions it is also found that small rare-gas atoms can sometimes be forced into the fullerene cage to form endohedral complexes [10].

At somewhat higher CM energies other collision phenomena become manifest. For example, at CM energies around 1 keV, collisions between C_{60}^+ and H_2 or He exhibit a ''power-law'' distribution of positively charged fragments and this has been interpreted as evidence for a model wherein the fullerene sphere is opened in a collision and pairs of carbon atoms evaporate before it closes again [12]. At CM energies around 100 keV, collisions between highly charged heavy ions and C_{60} show that the C_{60} can become

*Present address: Department of Physics and Astronomy, University of Toledo, Toledo, OH 43606.

†Present address: Department of Physics, University of Notre Dame, Notre Dame, IN 46556.

 © 1996 The American Physical Society

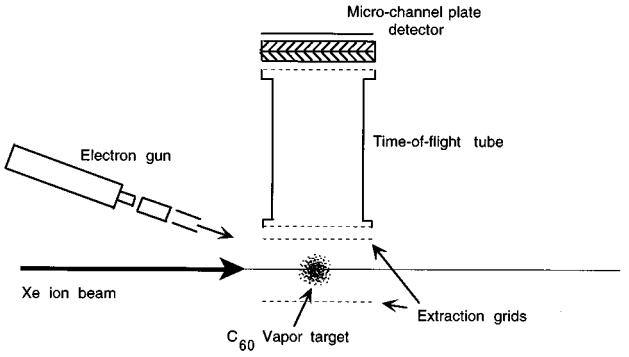

FIG. 1. Schematic diagram of the experimental arrangement.

ionized (sometimes multiply—C_{60}^{q+} with values of q up to 9 have been observed [15,16]) in large-impact-parameter collisions and then survive intact for at least several microseconds, whereas for close collisions the C_{60} is often catastrophically destroyed [17].

In the set of experiments described here, collisions between highly charged ^{136}Xe ions and C_{60} were studied at laboratory energies in the range 420–625 MeV (CM energies 353–526 MeV), several orders of magnitude above the energies used in previous collision studies. Additionally and in distinction from many previous measurements, coincidences between the various product fragments were measured. We expected and indeed found that the collision mechanisms at these high energies differ significantly from those that dominate at the lower energies. Some of this work has been described in abbreviated form in a previously published Letter [18].

II. EXPERIMENTAL DETAILS

The experimental arrangement is sketched in Fig. 1. A C_{60} vapor target was bombarded by a beam of positively charged ^{136}Xe ions from Argonne's superconducting heavy-ion accelerator, ATLAS, at (laboratory) energies in the range 420–625 MeV. In most of our measurements the Xe charge state was 35+ and the beam energy was 625 MeV. The vapor target was formed from 99.5% pure C_{60} powder [19] that was heated to temperatures in the range 470–520 °C in a two-stage stainless-steel oven [20] located at the base of the target chamber and enveloped in a heat shield. A cluster of nine separate 0.007-in.-diameter nozzles was located in a 0.115-in.-thick Mo plate on the upper surface of the oven. From previously measured vapor-pressure data [21] we estimated the C_{60} density in the oven at 475 °C to be approximately 1.2×10^{13}/cm^3 and in the target region to be about 10^{12}/cm^3. A cylindrical copper cold shield held at liquid-nitrogen temperature was located above the oven and surrounding the target region. This shield served to condense out most of the evaporated C_{60} that appeared as a yellowish-brown deposit on the copper. The shield had various apertures cut in it to permit passage of the beam, emergence of the detected fragments, etc. The background pressure in the target chamber (with the oven on) was typically around 2×10^{-7} Torr. Located above a small hole in the top of the cold shield was the quartz crystal of a thickness-monitor system, which served to indicate the rate of evaporation of the C_{60}. In the horizontal plane and at 90° to the incident beam direction was a time-of-flight (TOF) spectrometer system. Grids symmetrically located on both sides of the target region were biased with equal and opposite voltages to extract positively charged fragments and to inject them into a 20-cm-long gridded flight tube and then into a microchannel-plate detector (MCP). The response of MCP's is known [22] to be dependent upon factors such as the detected ion's mass and energy. After tests to determine and optimize the MCP's response to ions with masses up to 720 with various voltages on the TOF spectrometer, the measurements were performed with a total acceleration voltage of 6.9 kV. Fragment flight times ranged up to about 8 μs. As an added verification of the performance of the TOF system, a small amount of pyrene ($C_{16}H_{10}$) was sometimes added to the charge in the oven. This compound evaporated totally at around 160 °C and provided calibration peaks with mass-to-charge ratios, $M/Q=202$ (singly charged) and 101 (doubly charged).

The electron-cyclotron-resonance ion source of the ATLAS accelerator was fed with Xe gas enriched to 64% in ^{136}Xe (this isotope was chosen so as to minimize possible ''mass/charge'' ambiguities in the accelerator). In normal ''CW'' operation, beams from ATLAS emerge as pulses with a repetition rate of 12.125 MHz (period 82.5 ns). To facilitate the measurement of fragment flight times that ranged up to about 8 μs in the present experiments, a ''sweeper'' was employed in ATLAS to select just one beam pulse out of every 121 for delivery to our experiment. Thus the pulse period at the target position was about 10 μs. The pulse width was reduced through the use of a rebuncher to a value typically around 400 ps. Time-averaged beam currents measured (after reduction through application of the sweeper) in a Faraday cup downstream from the target were typically in the range 20–70 pA for Xe^{35+} beams.

TOF spectra were obtained using a ''multihit'' time digitizer with the ''start'' signal coming from the MCP and the ''stop'' signal from the accelerator's timing system. In this manner up to eight fragments (having flight times that differed by at least 3 ns) could be measured if they arose in coincidence from a single fragmentation event in the target. The TOF data for each event were partially sorted on line and were all written on magnetic tape for off-line analysis.

To characterize and monitor the vapor target in the absence of the Xe beam, an electron gun was built into the target chamber. The axis of this gun lay in the horizontal plane and 12° from the ion-beam axis. The acceleration voltage on the gun was 2.8 kV and this, in conjunction with the extraction voltages on the grids near the target, resulted in the electron beam being steered through the same target region that was illuminated by the ion beam. The electron beam was swept vertically over a slit in the cold shield to give short (~10 ns) pulses at the target. The TOF spectra obtained for the electron-induced ionization of C_{60} provided valuable confirmation that the target was functioning correctly. Peaks were seen corresponding to singly and doubly ionized C_{60}. Interestingly, no fragmentation peaks were observed, in contrast to some previous work [11,23] using electron beams but under somewhat different experimental conditions. Also seen were various ''contaminant'' peaks due to background gases (H_2O, N_2, O_2, CO_2, etc.).

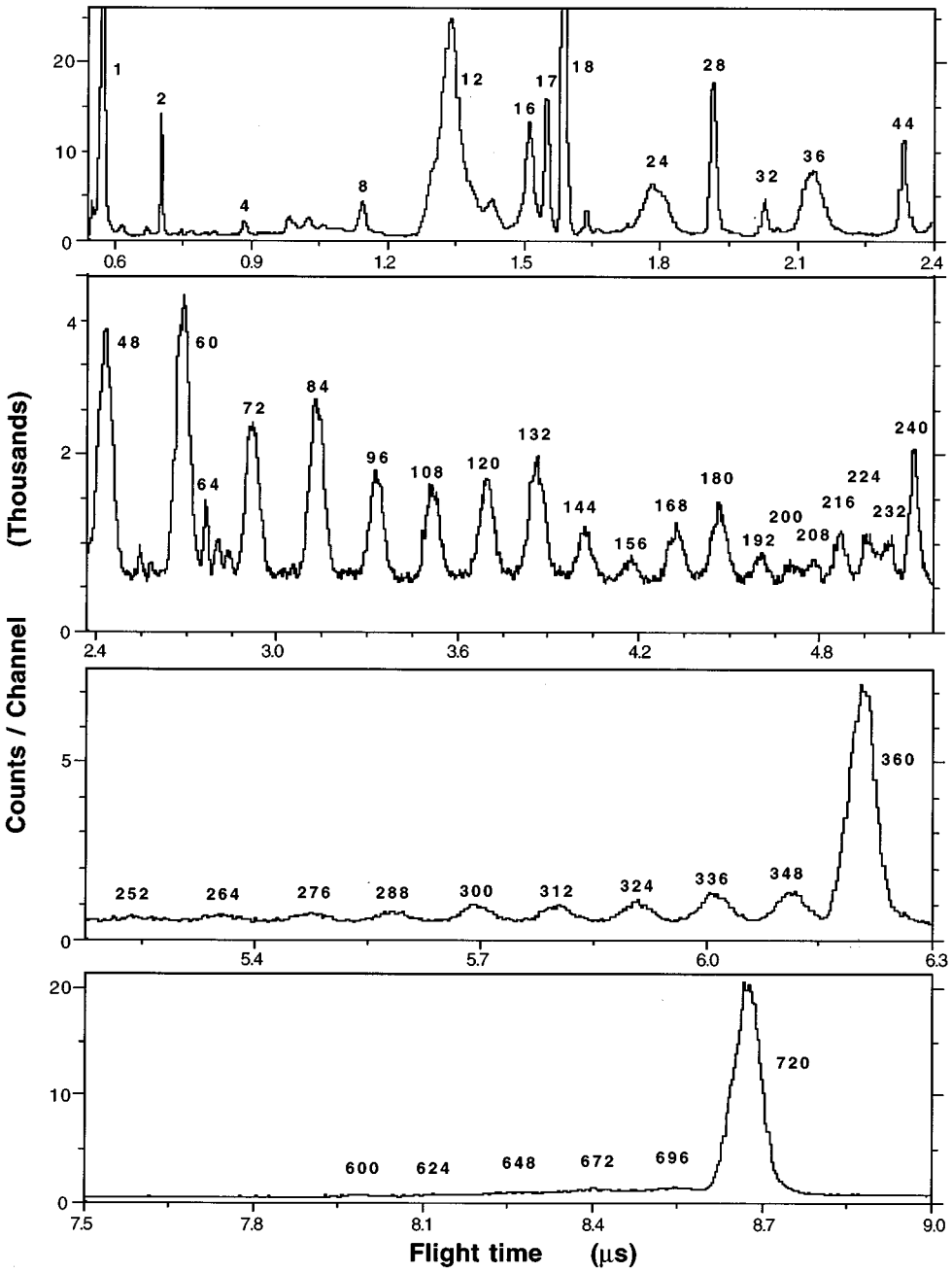

FIG. 2. Time-of-flight spectrum for positive fragments arising from bombardment of C_{60} vapor by 625-MeV $^{136}Xe^{35+}$ ions. The numbers given above the peaks are the ratios (M/Q) of fragment mass (amu) to charge.

III. RESULTS

A. General observations

Figures 2 and 3 show a TOF spectrum (and its equivalent calibration in terms of M/Q) obtained with an incident beam of 625-MeV $^{136}Xe^{35+}$ ions. These figures show the same TOF data that were published in Ref. [18] but with expanded time scales. The spectrum is the sum of all eight channels in the time digitizer and thus reflects the distribution for all of the positive fragments detected (events in which more than one positive fragment is produced are thus included). Positively ionized carbon fragments ranging from single carbon atoms up to C_{60} are observed. The absence of ionization states of C_{70} and higher fullerenes attests to the purity of the C_{60} target. Most of the peaks are fairly narrow and symmetric in shape, indicating that the emission of fragments is generally prompt and that the contributions from delayed processes (delay times greater than a few hundred nanoseconds) are relatively small.

The TOF spectrum exhibits peaks attributable to contaminant gases (H_2O, N_2, O_2, CO_2, etc.) that were present to some extent even when the oven was turned off. As we will show later, these peaks are useful for estimating the instrumental contributions to the carbon cluster peak widths. The peaks in the TOF spectra stand on an overall background level that is partly beam independent (due to random noise in the MCP) and partly beam dependent.

The width of a peak in the TOF spectrum is a measure of the original kinetic energies of the corresponding fragments. These effects have been described in detail elsewhere [24] and we will briefly summarize the aspects relevant to the analysis of these spectra. If field penetration at the grids is

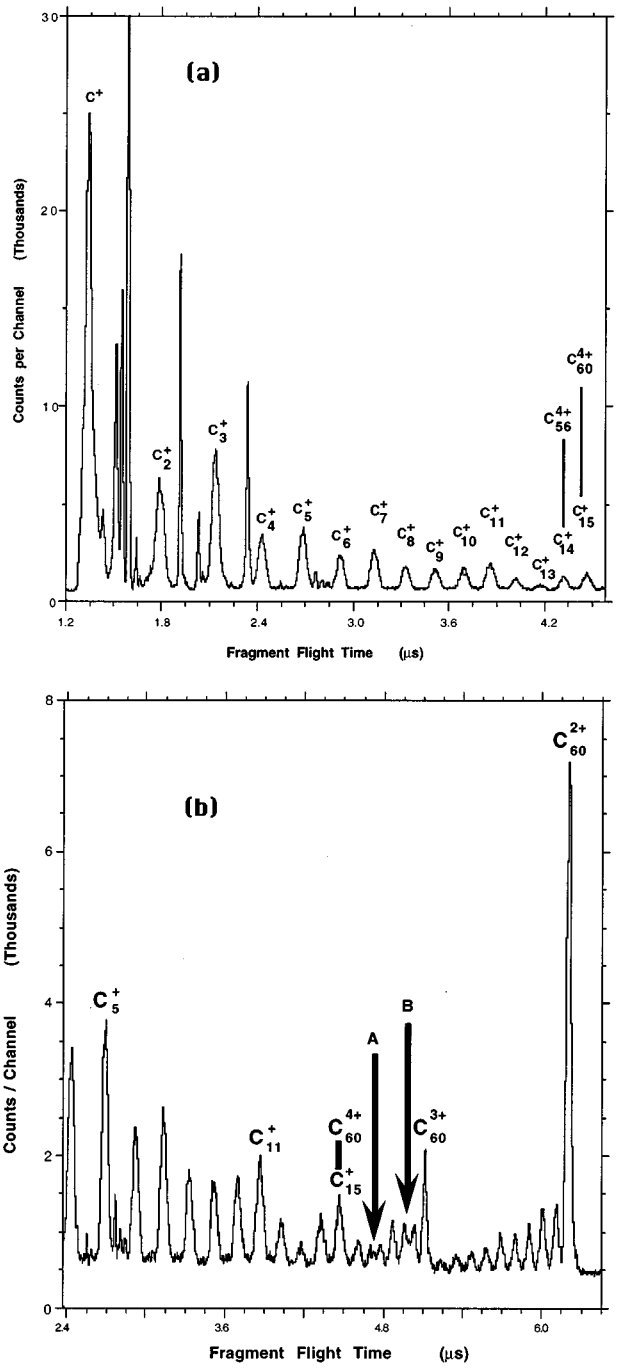

FIG. 3. Portions of the time-of-flight spectrum (Fig. 2) illustrating (a) the ''multifragmentation'' peaks and (b) the doubly and triply charged ENHM peaks and also the region of transition from linear to cyclic ring structures. The ''fill'' in the valleys labeled as *A* and *B* are due to C_{17}^{+} and C_{19}^{+}, respectively.

neglected, the flight times for a charged fragment in the various regions of the spectrometer can be calculated from the equations of motion for a particle under constant acceleration. To extract the relation between the broadening and the initial kinetic energy of the fragment (mass M and charge Q), the formula for the time of flight is expanded in a power series of the initial velocity of the fragment along the axis of detection. The change in the time of flight (Δt) relative to the center of the peak is found to be proportional to the initial momentum along the axis of detection:

$$\Delta t \approx -\frac{M v_{\parallel}}{Q\mathcal{E}}, \tag{1}$$

where $v_{\parallel}$ is the initial velocity parallel to the axis of detection, and $\mathcal{E}$ is the strength of the electric field in the interaction region. To estimate the contribution to the width from thermal velocities we can use this to convert the Maxwell-Boltzman velocity distribution, which is Gaussian in one direction, to a time distribution. Extracting the full-width at half maximum (FWHM) yields

$$\mathrm{FWHM}_T = \frac{\sqrt{(8\ln 2)MkT}}{Q\mathcal{E}}. \tag{2}$$

The peaks observed in the time-of-flight spectrum will be broadened by the thermal velocities of the target molecules, the kinetic energy released in the fragmentation process, and the spatial extent of the source, which is not completely compensated by the space focusing. The above formula can be used to estimate the thermal broadening.

In Figs. 2 and 3, the peaks due to singly, doubly, triply, and (possibly) quadruply ionized C_{60} (which we refer to as the ''parent peaks'') are clearly visible and their relative intensities decrease towards higher charge states. The widths of the C_{60}^{+} and C_{60}^{2+} peaks are 58.1 and 41.8 ns, respectively, in principle resulting from the source size and thermal broadening because no fragmentation occurs. The thermal broadening of the C_{60}^{+} peak is calculated to be 17 ns using the above formula and 20 ns using a complete expression for Δt. Source broadening is estimated to be smaller ($\sim$5 ns), demonstrating that instrumental factors such as field penetration also contribute strongly to the resolution at high masses.

Because the TOF technique separates ionic fragments according to M/Q, there can be ambiguities in assigning masses and charges to the various peaks observed. So, for example, the ions C_{60}^{4+}, C_{45}^{3+}, C_{30}^{2+}, and C_{15}^{+} would all have the same flight times corresponding to $M/Q=180$. The systematics of the various peak intensities and also the coincidence information can help resolve many of these ambiguities. Thus the systematic trend in the peak intensities for the observed singly charged fragments C_n^{+} coupled with the trend in the peak intensities for the ionization states of the parent ions C_{60}^{q+}, leads us to believe that most of the intensity in the peak at $M/Q=180$ is due to the fragment C_{15}^{+}. The absence of a peak at $M/Q=270$ (that would correspond to C_{45}^{2+}) indicates the improbability that the $M/Q=180$ peak contains any contribution from C_{45}^{3+}. The coincidence data and also the ''even-numbered high-mass'' (ENHM) peaks (see below) do not suggest the presence of $n=30$ fragments to any significant degree and this in turn suggests that the $M/Q=180$ peak does not contain any significant contribution from C_{30}^{2+}. Similar arguments can be made in helping to resolve ambiguities in peaks corresponding to other values of M/Q.

Also clearly to be seen in Figs. 2 and 3 are the ENHM peaks (C_{58}^{q+}, C_{56}^{q+}, C_{54}^{q+}, etc) corresponding to the losses of even numbers of carbon atoms. For the higher charge states these ENHM peaks are stronger relative to their parent

peaks than in the case of singly charged ions. These peaks should be wider than the associated parent peak because kT is only of the order of 50 meV at our oven temperatures (500 °C), while we expect substantially more energy release from a fragmentation event, even for a neutral dissociation such as this. These peaks are indeed wider, with the singly charged and doubly charged fragments exhibiting widths of about 92 and 49 ns, respectively. These widths are found to remain constant within our accuracy for the different ENHM peaks, corresponding to a few tenths of an eV. Given the instrumental uncertainties discussed earlier, it is difficult to extract precise energies.

One sees from Fig. 2 that the peaks corresponding to singly charged ENHM fragments are ''blurred'' together. Although this suggests that these fragments may be produced with time delays up to a few hundred nanoseconds it should be noted that the ''blurring'' phenomenon was not present in all of the TOF spectra. There may be an effect due to other factors such as oven temperature, focusing fields, etc.

The TOF spectrum also illustrates a noteworthy feature that is unique to these high-energy fragmentation studies, namely, the pronounced occurrence of the sequence of singly charged fragments C_n^+, with n assuming all values from 1 to at least 19 (peaks corresponding to higher values then become indistinguishable from the multiply charged ENHM peaks). These peaks alternate in intensity up to around $n=9$ with the odd-numbered peaks being more intense than the even numbered. This alternating pattern of peak intensities is, to our knowledge, unique among fragmentation studies, but it mirrors the fragment yields found upon evaporation of graphite in a discharge (see, for example, Refs. [25 and 26]). The distribution of cluster yields from a discharge reflects the relative stability of the different clusters as a function of size. It appears that the elevated excitation energies, which result in generation of the small carbon fragments here, are necessary to reach a regime of excitation where the distribution of cluster sizes is largely determined by the relative stabilities of the fragments. This stands in contrast to other fragmentation studies, which do not observe the limiting behavior of a discharge and are presumably more dependent on the details of the excitation process. As can be seen in Fig. 3(b), above $n=9$, the most intense peaks appear to be $n=11$, 15, and probably 19 (the ''fill'' in the ''valley'' between the C_{56}^{3+} and the C_{58}^{3+} peaks is almost certainly due to the presence of C_{19}^+). The (smaller) peak for $n=17$ fills in the valley between the C_{50}^{3+} and the C_{52}^{3+} peaks, while those for $n=18$, 20, 21, 22, etc. coincide with various multiply charged ENHM peaks as indicated in Fig. 3(b). We refer to this series of peaks, C_n^+ ($n=1$ to ~ 20) as the ''multifragmentation'' peaks, since we believe that they arise predominantly from events in which there is a catastrophic disintegration of the C_{60} molecule into many small fragments.

B. Dependence on ion-beam energy

In order to investigate the energy dependence of the ionization and fragmentation processes, time-of-flight spectra were taken with Xe^{18+} ions at a number of laboratory energies in the range 420–625 MeV. Energy variation was achieved by switching resonators off or on in the linac. Each energy change was accompanied by a retuning of the beamline optical components. There was a slight shift of the TOF spectrum at each energy because of the difference in the beam arrival time at the target chamber relative to the master clock of the linac. This shift was readily removed in the data analysis. The yields at each energy were normalized to the integrated charge collected by a Faraday cup located downbeam from the target. The possibility of small changes in ion trajectories through the jet target in addition to an uncertainty in correcting for offsets in the Faraday-cup integrator contributed to the overall uncertainty in these measurements. We found the yield to be about 7.5×10^{-6} C_{60}^+ ions detected per incident Xe^{18+} ion over the energy range studied and it was roughly constant within the experimental error. The C_{60}^+ ion yield as a function of the bombarding ion energy is shown in Ref. [18], Fig. 2(b).

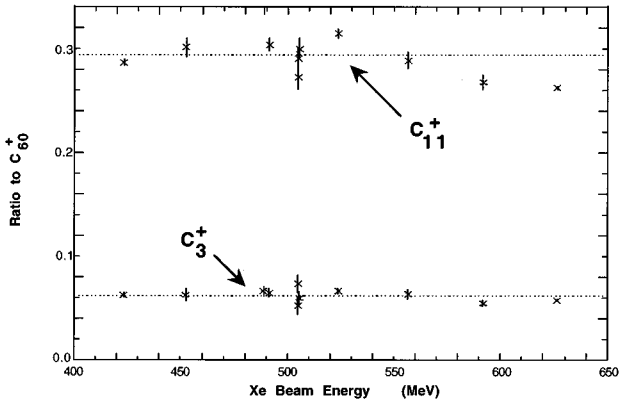

FIG. 4. Dependence upon bombarding energy of the yields (relative to C_{60}^+) of C_3^+ and C_{11}^+.

We also analyzed the yields of various other fragments as a function of beam energy. Figure 4 presents data on the yields of C_3^+ and C_{11}^+ normalized to that of C_{60}^+. Normalization to the C_{60}^+ counts, as has been done here, serves to eliminate some of the errors associated with beam tuning and beam-current normalization. Clearly there is little dependence on the beam energy. A similar lack of variation with bombarding energy was observed for C_{60}^{2+} and C_{58}^{2+} fragments. The C_{60}^{2+} yield was found to be about 22% of the C_{60}^+ yield and the C_{58}^{2+} yield about 2% of the C_{60}^+ yield.

C. Coincidence measurements

The widths of the peaks due to small carbon clusters indicate that the fragments are frequently created with large kinetic energies. This can be seen in Fig. 3(a) where the widths of the peaks for C_1^+ through C_3^+ ($M/Q=12,24,36$) are much wider than for the neighboring peaks from background gases (e.g., H_2O at $M/Q=18$). Fortunately the values of the kinetic energies can be extracted from these peaks more reliably because the instrumental contributions to the width are smaller for low masses, as can be seen from examination of the peaks due to the background gas. The transverse size of the source volume in our apparatus is determined by the width of the ion beam, and thus is the same for the carbon peaks and for the background gas. In addition, the temperature of the background gas is similar to that of C_{60} because most of the background gas is evolved from the oven. Therefore the instrumental broadening of the small carbon fragment peaks is indicated by the neighboring back-

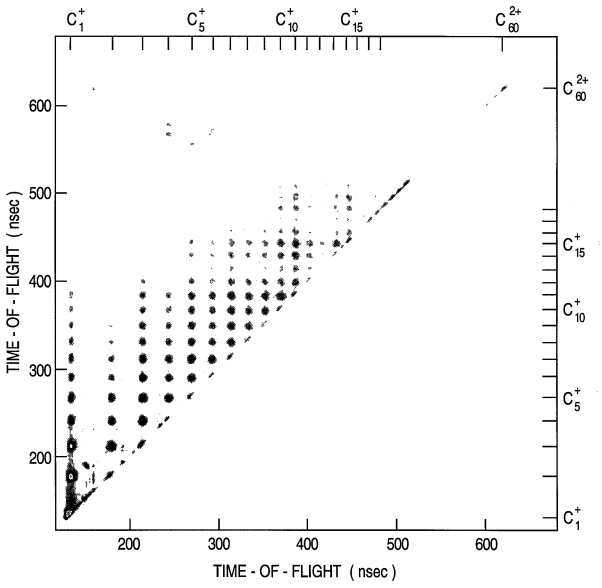

FIG. 5. Raw coincidence spectrum for events where only two fragments are detected. The horizontal axis represents the time of flight (TOF) of the first fragment detected and the vertical axis gives the TOF of the second fragment. No coincidence events are found outside of this window, other than random coincidences. The intensity contours correspond to a logarithmic scale.

ground gas peaks (those corresponding to ionization without fragmentation), the widths of which range from about 10 ns for H_2O to roughly 20 ns for CO_2. The carbon peaks are much broader, ranging from 46 ns for C_1^+ to 55 ns for C_4^+, demonstrating that the widths do not vary rapidly even over a fourfold change in mass. To estimate the corresponding fragment energies, the widths of the background gas peaks are subtracted from the carbon peak widths to account for the instrumental broadening. Calculations show that the underlying assumption (that instrumental and energetic contributions to the peak widths simply add) is valid to better than 10% for the accuracy of the fragment energies measured here. The variation in the widths of the carbon peaks is reduced even more after the instrumental widths are subtracted. The widths being roughly constant implies that on the average the same magnitude of momentum is imparted to each fragment. Note that while the momenta are roughly equal, the energies of the fragments are very different. Analysis of the measured peak widths gives an average energy for each fragment of approximately 60 eV/n, where n is the number of carbon atoms. (Multiply charged clusters were omitted from this analysis.)

As noted above, the use of a ''multihit'' time digitizer enabled us to measure in the TOF spectrometer as many as eight positive fragments from a given dissociation event, provided that their flight times differed from each other by more than 3 ns. Figures 5–8 show some specific detailed sections of the twofold coincidence array. It should be noted that while these data pertain to cases in which only two fragments were actually detected, they also presumably include events in which several positive fragments were generated, but not all detected, a consequence of the modest detection probability (typically in the range of 20–40 %) inherent in the TOF detector system. Random coincidences were held to a minimum (typically less than 5%) during the running of the experiment by keeping the instantaneous count rates low but commensurate with the need to acquire statistical accuracy.

The coincidence data show no evidence of charged fragments arising in coincidence with the singly charged ENHM peaks discussed in Sec. III A. Figure 5 shows a portion of the two-dimensional histogram of the total mass yield for all

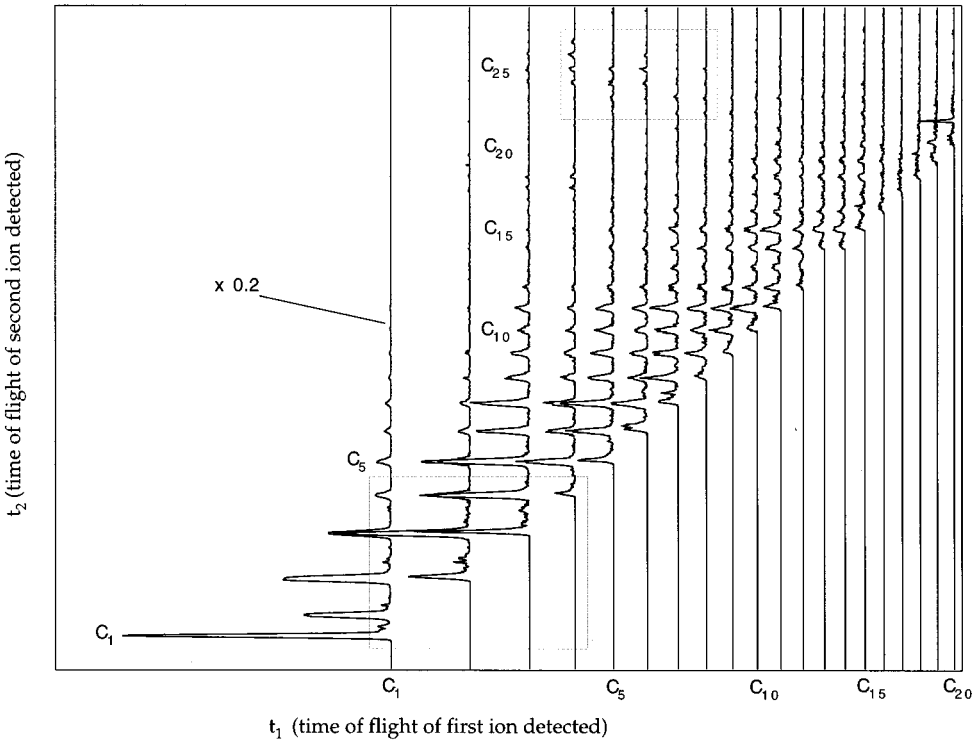

FIG. 6. Same spectrum as Fig. 5, histogrammed to show fragment yields. The lower and upper boxes highlight regions that are expanded in Figs. 7 and 8, respectively.

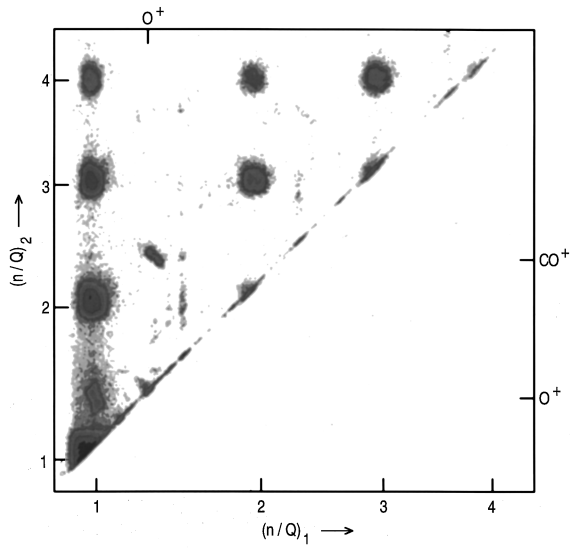

FIG. 7. Contour plot of the region of Fig. 6 corresponding to coincidences between two small carbon clusters. Axes are labeled in n/Q where n is the number of carbon atoms. The contour spacing is logarithmic.

events where two fragments are detected. Mass-to-charge ratios above 30 are not included in Fig. 5 because no real coincidences are observed outside the region shown. This indicates that under our conditions no singly charged ENHM peaks are detected in coincidence with any other fragments, apart from random coincidences. Therefore the singly charged ENHM peaks found near the C_{60}^{+} peak in Fig. 2 stem only from the loss of even numbers of neutral carbon atoms from the parent ions. However, a small number of peaks corresponding to doubly charged ENHM fragments are detected in coincidence with small odd- and even-numbered carbon fragments as discussed presently in the section relating to Fig. 6.

From Figs. 5 and 6 one notes that the multifragmentation peaks are, for the most part, observed in coincidence with

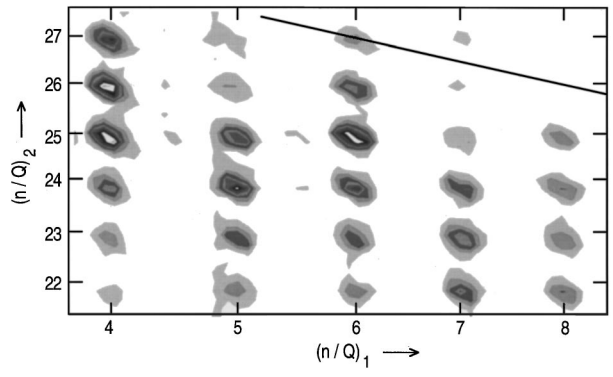

FIG. 8. Contour plot of the region of Fig. 6 corresponding to coincidences between one large doubly charged carbon cluster and one small cluster. Axes are labeled in n/Q where n is the number of carbon atoms. The diagonal line indicates peaks for which all 60 carbon atoms are detected. Although no real coincidences are observed above this line, the logarithmic contour spacing accentuates a spurious contribution from random coincidences at $(n/Q)_1=7$ and $(n/Q)_2=27$, providing an estimate of the background.

other multifragmentation peaks. That these fragments arise principally from many-body events becomes clearer when the contours of the coincidence peaks are studied in more detail. We will focus on the two regions highlighted in Fig. 6, because they are representative of the two types of behavior found in the coincidence spectra: (a) multifragmentation, which dominates the spectrum and for which a portion is shown in the lower region designated in Fig. 6, and (b) few-body breakup, which is shown in the upper region. The lower region is shown in more detail in Fig. 7, and the upper region is shown in Fig. 8. In the discussion that follows, it is important to keep in mind that the double coincidence spectrum includes contributions from processes that generate any number of fragments, because there is a finite chance that only two of the charged fragments are detected.

The multidimensional coincidence spectra, such as shown in Fig. 7, allow us to extract not only the momentum of each particle, but also the correlations between the momenta of the different fragments. For example, if a molecule breaks up into two charged fragments A and B, the two fragments have equal and oppositely directed momenta. If fragment A arrives 10 ns later than it would for zero initial velocity, it has been ejected away from the detector. Therefore fragment B will arrive 10 ns earlier than its nominal flight time. This simple result holds despite the fact that the flight times of the two fragments are, in general, very different, and is a consequence of the fact that time deviation is proportional to the momentum as indicated earlier. The foregoing shows that for two-body breakup the peak contour will be a straight line with the peak width reflecting the energy released to the fragments and the slope of the line being equal to $-Q_1/Q_2$. This is illustrated in Fig. 7 where the breakup of the background gas CO_2 into O^+ and CO^+ gives a peak $[(n/Q)_1=16/12;\ (n/Q)_2=28/12]$ with a linear contour and a slope of -1. If a third body is ejected in the fragmentation process, it modifies the observed peak shape. To the extent that the momentum of the third particle is parallel to the first two, the coincidence peak will remain linear but the slope will be changed. A fragment ejected perpendicularly to the two detected fragments will broaden the observed peak to an ellipsoidal shape. In practice there will not be only one undetected fragment but several, and the momenta will not be represented by well-defined values but by distributions. This results in a rich variety of peak shapes, from which one can infer details of the time development of the fragmentation process [24,27,28]. Some of these effects are illustrated in Fig. 7 where the peaks resulting from coincidences between small carbon fragments are very rounded, indicating that the unobserved mass—presumably many small carbon clusters—carries away a great deal of momentum. As a result, we expect that these peaks in the double-coincidence spectrum result primarily from processes that generate many charged carbon fragments—multifragmentation. This is borne out by the higher-order coincidence data where the mass yields for multiplicities two and higher are similar, with the bulk of the yield slowly shifting to lower masses as the multiplicity increases. It is interesting to note that the C^+/O^+ peak $[(n/Q)_1=1;\ (n/Q)_2=16/12]$ clearly shows the effects of a third fragment, demonstrating that these coincidences result from fragmentation of CO_2.

Another type of fragmentation process is also visible in the coincidence data, although it is rare compared to multifragmentation. In Fig. 6 an anomalously intense series of peaks found for $(n/Q)_2 \sim 25$ is highlighted in the upper box. In these events, one observes fragments with $(n/Q)_1$ in the range from 4 to 8 in coincidence with fragments with $(n/Q)_2$ in the range from ~ 22 to ~ 28. Figure 8 shows a more detailed contour display of some of the peaks in this region. Here the peak contours are much more linear than for the case of multifragmentation and clearly result from few-body breakup. Thus, for example, the coincidence peak in Fig. 8 that corresponds to $(n/Q)_1=6$ and $(n/Q)_2=25$ has a slope of -0.5 and therefore $Q_2/Q_1=2$. So this peak arises from a process in which C_{50}^{2+} and C_6^+ are the two main fragments produced together with the possible emission of a small number of light fragments, such as carbon atoms and electrons. A whole series of such peaks is visible in Fig. 8, and result from weak processes wherein a C_{60}^{Q+} ion of charge state 3 or higher splits into a large doubly charged even-mass fragment plus a few very small carbon clusters. These events are not unlike those observed by Scheier, Dünser, and Märk [16], but in contrast to their results we find very few events where two fragments account for all of the original mass, and no C_{58}^{2+}/C_2^+ events can be distinguished above background. This is illustrated in Fig. 8 where peaks corresponding to detection of all 60 carbon atoms would fall on the diagonal line in the upper-right corner of the spectrum. Clearly most of the events in this part of the spectrum include two to four undetected carbon atoms. It should be kept in mind that the experiment described here is somewhat different from that of Scheier, Dünster and Märk, which may explain the contrasting results. For example, C_{60}^{3+} fragments which fission into C_{58}^{2+}/C_2^+ after a microsecond or so would be detected in the parent peak in our spectra. But it is clear that while our results manifest few-body breakup processes for C_{60}^{Q+} ions of charge state 3 or higher, such processes yield both odd- and even-numbered small carbon fragments. In addition, such processes are statistical, usually generating at least two small fragments. Thus, singly charged ENHM clusters such as C_{58}^+, C_{56}^+, etc. are not found in coincidence with any other charged fragments. However, (presumably more energetic) processes that yield C_{60}^{Q+} for charge states of 3 and higher do begin to share the positive charge with the smaller emitted fragments.

IV. DISCUSSION

The interaction mechanism and the energy transfer in the collision of a fast highly charged heavy ion with C_{60} can be expected to depend strongly on the impact parameter of the collision. One of the distances of principal importance in discussing impact parameters is the mean radius R of the hollow truncated-icosahedral C_{60} ''cage'' on which are located the time-averaged positions of the nuclei of the 60 constituent carbon atoms. This distance is known [2] to be 3.55 Å. In comparison, the ''diameter'' of a Xe^{35+} projectile is about 0.2 Å and thus for our purposes may be treated as a point particle. For impact parameters (measured relative to the center of the molecule) on the order of R or smaller, one has to consider the possibility of collisions with individual carbon atoms in the molecule. The probability of such collisions resulting in the direct ''knock out'' of individual carbon atoms is expected to be relatively small since impact parameters on the order of 0.1 Å or less (measured with respect to individual carbon atoms) are necessary in order to impart the few eV of energy required to eject a constituent carbon atom. In contrast to the process of direct ejection of individual carbon atoms or ions, a much more probable mechanism is that in which the projectile deposits a large amount of energy into the target molecule via electronic excitation, which then leads to electron loss and/or fragmentation. The impact parameter plays a crucial role in determining the type of electronic excitation. For large impact parameters, as shown below, the dominant mode of excitation is expected to be through the giant dipole plasmon resonance (GDPR) that has been predicted [29] and measured [30,31] to have an energy of about 20 eV and a full width a half maximum (FWHM) of about 10 eV in the C_{60} molecule. For small impact parameters where the projectile actually traverses the molecule, a reasonable approximation would be to view the process as a stopping-power phenomenon and to describe it in terms of the formalism used in the theory of energy loss for fast ions traversing solids.

In both extremes of the range of impact parameters, considerable insight can be gained from treating the target molecule as a ''jelliumlike'' solid shell (also known [32] as ''shellium''). In this approximation one views the C_{60} molecule as containing a positively charged ''core'' of sixty C^{4+} ions whose charges and masses are ''smeared out'' over a spherical shell of radius 3.55 Å and thickness about 0.2 Å, reflecting the radius of the K shell in carbon and also the fact that the tightly bound K-shell electrons play a very minor role in the absorption of energy. The excursions of the carbon nuclei in their thermal vibrations will be on the same order of magnitude as the shell thickness. For each carbon atom the four valence electrons are hybridized into sp^2 configurations with three strong σ bonds and one weaker π bond. Thus in the entire molecule the 240 valence electrons are partitioned into 180 σ electrons, which are relatively tightly bound, lie close to the positively charged shell core, and are mainly responsible for the molecular binding and into 60 more weakly bound π electrons, which lie mainly on the inner and outer surfaces of the C_{60} cage and extend from a molecular radius of about 2 Å out to about 5 Å. This is consistent with the observation [3] that C_{60} condenses as a van der Waals crystal with a 10-Å spacing between centers of nearest-neighbor molecules. It is also consistent with more refined calculations of the radial distribution of electron density (see, for example, Refs. [33–35]).

The valence electrons in C_{60} participate in collective excitations. The properties of these excitations have been calculated in linear-response theory by Bertsch and co-workers [29,36] who predicted several resonances in the 3–6-eV range and also a giant plasmon resonance at about 20 eV Barton and Eberlein [37] (using a hydrodynamic model) and Amusia and Korol [38] have made similar predictions. These calculated properties have been confirmed experimentally. For example, the high-resolution electron-energy-loss measurements of Gensterblum *et al.* [39] on thin films of C_{60} revealed these excitations in the solid state, and similar techniques employed subsequently in the gas phase by Keller and Coplan [31] displayed two prominent regions of excitation:

one around 6 eV (thought to be predominantly a π resonance) and one around 20 eV (thought to be a giant dipole plasmon resonance excitation involving mostly σ electrons). The GDPR was also observed [30,40] strongly and cleanly in photoionization experiments.

The time for a 625-MeV Xe ion to traverse 10 Å, a distance corresponding to the ''outer diameter'' of the C_{60} molecule, is 3×10^{-17} s. This is short compared to the period for any internal rovibrational mode in the molecule. Furthermore, the high velocity ($\sim 14v_0$) is large compared to the velocities ($\sim v_0$) of valence electrons in the target molecule and also to the orbital velocities ($\sim 6v_0$) of the fastest target electrons, the *K*-shell electrons. This is the main reason for the low probability for direct electron capture from the target molecule by these swift highly charged projectiles [41]. In this respect the situation is quite different from that in the various experiments conducted at low collision energies. For example, in our measurements the xenon projectile velocities are about 50–100 times higher than in those employed by Walch *et al.* [17] and the electron-capture cross sections are correspondingly about a factor of 100 smaller [42].

For larger impact parameters the collision interaction times become longer and it becomes possible for the projectile to couple strongly with the various collective excitations in the molecule. At still larger impact parameters the excitation probability drops off again because (a) the Coulomb interaction becomes weaker, and (b) the collision times become large compared to the period of the excitation and the interaction becomes adiabatic. An estimate of the impact parameter at which this occurs is Bohr's adiabatic distance [41], $b_0=\gamma\hbar v/E$, where γ is the usual relativistic parameter, v is the projectile velocity, and E is the energy of the excitation. This has the value 10 Å for 625-MeV Xe ions, assuming $E=20$ eV for the excitation of the GDPR.

We consider now the excitation of the giant resonance by the Coulomb field of the xenon projectile. The effective number of plasmon excitations at an impact parameter b is

$$N(b)=\int dE\,\frac{f(E)}{E}\,\frac{2Z_P^2e^4}{mv^2}\,\frac{1}{b^2}\left[\xi^2K_1^2(\xi)+\frac{1}{\gamma^2}\,\xi^2K_0^2(\xi)\right], \tag{3}$$

where $\xi=Eb/\gamma\hbar v$, $f(E)$ is the oscillator-strength distribution, Z_P is the charge state of the xenon ion, and K_0 and K_1 are modified Bessel functions. This expression, which is obtained in first-order perturbation theory, is based on that for the average energy transfer to a harmonic oscillator [43]. The predicted [29,36] integrated oscillator strength for the resonance is about 70. In evaluating Eq. (3), we approximate the oscillator-strength distribution $f(E)$ as a Gaussian normalized to reproduce the oscillator strength, the width, and other known parameters of the resonance. The quantity $N(b)$ thus evaluated is shown in Fig. 9. One sees that $N(b)$ becomes large for $b\lesssim R$ (a value of 100 corresponds to an energy deposition of 2 keV). In deriving Eq. (3) it is assumed that the GDPR can be treated as a point oscillator. Clearly, this and other assumptions (e.g., linear response, dipole approximation, etc.) will be expected to break down at small impact parameters. However, for impact parameters on the order of 10 Å or more, these approximations can be expected to have reasonable validity.

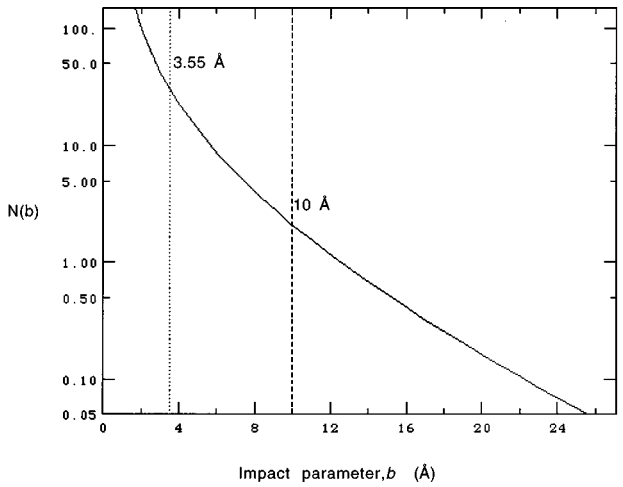

FIG. 9. Effective number of plasmon excitations [Eq. (3)] as a function of impact parameter for 625-MeV $^{136}Xe^{35+}$ ions incident on C_{60}.

As Fig. 9 suggests, the strength of the plasmon resonance, combined with the high charge state of the xenon ion, implies also that multiple excitations play an important role even at distances as big as the adiabatic distance b_0. To make a realistic estimate of cross sections, we describe the plasmon excitations in terms of a ''coherent state'' [44]. The multiplasmon excitation probabilities are then given by a Poisson distribution generated by $N(b)$. In particular, the probability for a one-plasmon excitation is $N(b)\exp[-N(b)]$, and the total excitation probability is $1-\exp[-N(b)]$. These two probabilities are illustrated in Fig. 10. For comparison we show in Fig. 11 the excitation probabilities for multiple plasmon excitations (up to four). As noted above, we expect the model to break down as the number of excited plasmons increases. Figures 9 and 11 suggest that it would be unwise to trust details of the model to much more than the first two plasmon excitations. However, since the total excitation probability reaches unity at an impact parameter of about 7 Å (Fig. 10), and since this is still well outside the radius R, one can expect to be able to derive a realistic value for the total interaction cross section.

To determine the total interaction cross section, it is therefore not necessary to consider explicitly reactions at the

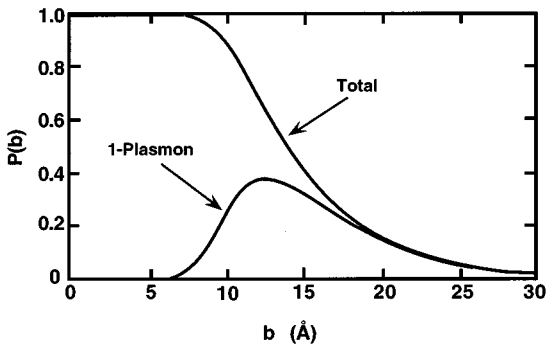

FIG. 10. Calculated probabilities for the total interaction and for single-plasmon excitation as functions of the impact parameter b.

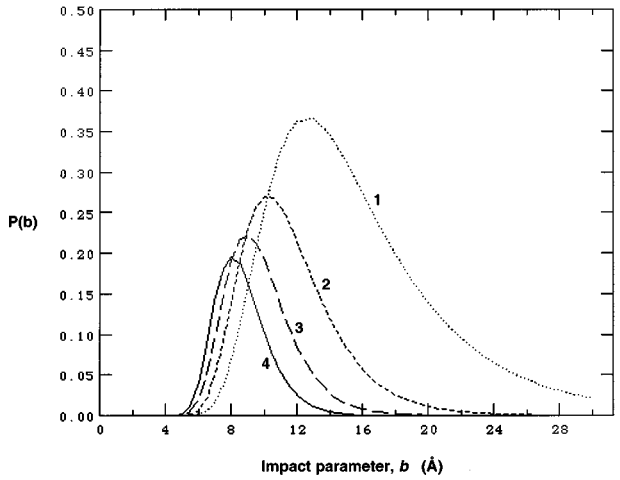

FIG. 11. Calculated probabilities for multiple plasmon excitation (one through four plasmons) as functions of the impact parameter b. The figures by the curves indicate the number of plasmons excited.

smaller impact parameters where the xenon ion may interact in complicated ways both via coherent excitations and with individual electrons. We can simply write this cross section as

$$\sigma_{\rm exc}=2\pi\int_0^\infty db\ b\{1-\exp[-N(b)]\}. \tag{4}$$

The single-plasmon excitation cross section can be derived in a similar way as

$$\sigma_{\rm 1pl}=2\pi\int_0^\infty db\ bN(b)\exp[-N(b)]. \tag{5}$$

These estimates are reasonable since essentially all of the cross section comes from impact parameters significantly larger than R (cf. Fig. 10). The total interaction cross section obtained from the calculated values shown in Fig. 10 is 811 Å^2, and the single-plasmon cross section is 387 Å^2, i.e., 48% of the total.

The physical mechanism and the theoretical description that we employ have interesting parallels in nuclear physics. For example, in experiments [45,46] conducted at GSI, Darmstadt, relativistic (0.7-GeV/A) beams of ^{136}Xe were collided with Pb targets. In peripheral collisions the electromagnetic excitation probabilities are very high and the single and double excitations of the collective nuclear giant dipole resonance are clearly seen. In describing their results the authors use the Weizsäcker-Williams method of virtual photons that is equivalent to the approach we employ here [43].

The dominant decay mode of the single-plasmon excitation in C_{60} is thought to be via electron emission [30,47]. We therefore compare the calculated single-plasmon cross section [Eq. (5)] to our measured C_{60}^+ yield. The dependence on beam energy was illustrated in Ref. [18] for the projectile charge state $Z_p=18$. The weak dependence on beam energy is reproduced by the calculation.

Because of the dominance of the GDPR and because higher multipole excitations are not well documented either theoretically or experimentally, we have not attempted to take these higher multipoles into account in our description. It will be interesting to do so as further clarification of these expected excitations occurs. Possible theoretical approaches are indicated by the work of Ferrell and Echenique [48] and references contained therein.

Since the interaction probability becomes essentially unity for impact parameters less than about 7 Å (Fig. 10) and the energy deposition becomes large (Fig. 9), practically all projectile-target interactions in this range of impact parameter can be expected to result in fragmentation. We have constructed a bond-percolation model to describe these fragmentation processes. In the model C_{60} is represented as a collection of lattice sites located at the positions of the carbon atoms. Each site is connected to its three nearest neighbors via bonds. (In this calculation we do not distinguish between the 60 ''single'' and 30 ''double'' bonds, which have lengths of 1.45 and 1.40 Å, respectively [3].) We adopt a Monte Carlo approach. We assume that a beam of xenon ions uniformly illuminates a C_{60} molecule target and that each xenon ion deposits a calculable amount of excitation energy into the molecule. This energy is then assumed to be rapidly distributed in a uniform manner over the whole C_{60} cluster leading to the breaking of individual bonds. All bonds are assumed to be equivalent and they each break with a probability that is directly proportional to the total energy deposition (which in turn, is dependent on the impact parameter). We use a random-number generator to determine whether a given bond breaks or not. Thus for each projectile, knowing which C_{60} bonds are broken, we can calculate the masses of the fragments thereby generated.

For the purpose of determining the energy deposition, we adopt the approach mentioned above and represent the hollow fullerene structure as a spherical shell of ''jellium'' with mean radius R and half-width ΔR. The impact-parameter dependence of the bond-breaking probability is given by

$$p(b)=\frac{p_0}{2\sqrt{\pi}w\Delta R}\int dr_\perp\{\sqrt{[(R+\Delta R)^2-r_\perp^2]_+}-\sqrt{[(R-\Delta R)^2-r_\perp^2]_+}\}\exp[-(b-r_\perp)^2/w^2], \tag{6}$$

where we have introduced the symbol $[a]_+\equiv a$ $(a\geq 0)$, $[a]_+\equiv 0$ $(a<0)$. w is the effective transverse width of the projectile and p_0 is the bond-breaking probability in collisions in which $b=0$.

After computing the breaking of the bonds by a given projectile, we employ a cluster recognition algorithm and identify the sites still connected via unbroken bonds as members of a cluster. We record the size of each cluster and, to mirror the experimental situation, we assume that there is a detection efficiency of 20% for each cluster. This model is, except for considerations of the different reaction geometries involved, similar to a model of nuclear multifragmentation [49–51] used to explain production cross sections [52] for nuclear fragments emerging from heavy nuclei bombarded by protons with energies between 80 and 300 GeV.

Figure 12 shows the fragment-mass distribution calculated using this model and with parameters $\Delta R=0.35$ Å,

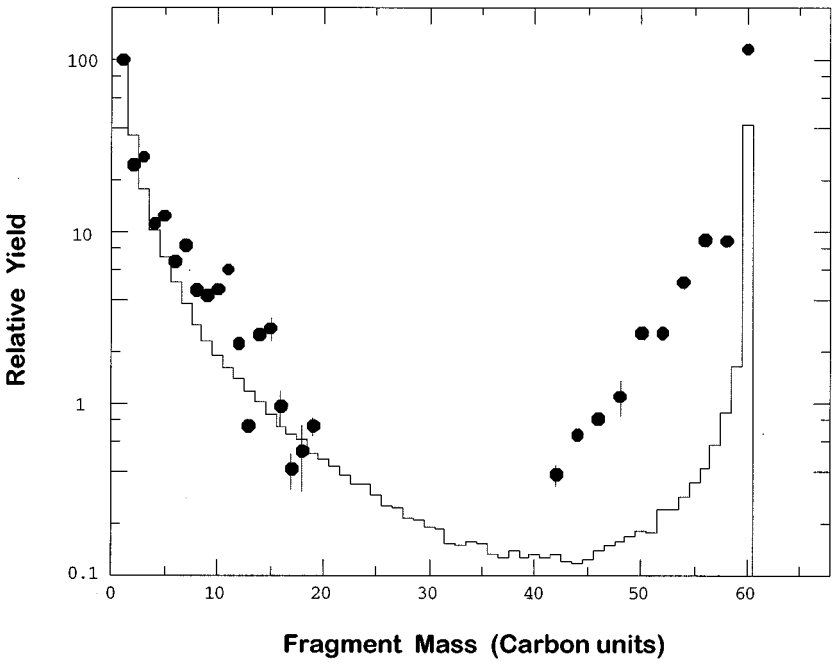

FIG. 12. Measured mass distribution (solid points) for positive fragments arising from C_{60} bombarded by 625-MeV $^{136}Xe^{35+}$ ions. The histogram is the distribution calculated on the basis of a multifragmentation model (see text). The fragment detection efficiency was taken to be 20%. The error bars are smaller than the points except where shown. The errors reflect statistical fitting errors and also any ambiguities in M/Q values (see Fig. 3). (The absence of experimental points for fragment masses between ~20 and ~40 is due to ambiguities of this sort.)

$w=2$ Å, and $p_0=0.5$. Our calculation reproduces the overall shape of the measured fragment mass spectrum. The calculation gives too little yield at high mass numbers because it does not take into account (a) the contributions from evaporative processes in which electrons and/or neutral carbon fragments are emitted following more gentle excitations (e.g., plasmon excitations), and (b) the known instability of odd-numbered heavy fragments that decay rapidly into even-numbered ones. The comparison shown in Fig. 12 assumes that the positive fragments are representative of all fragments emitted.

Our coincidence measurements demonstrate that the fragments with more than 40 carbon atoms shown in the right-hand portion of Fig. 12 are not detected in coincidence with the lighter fragments shown in the left-hand portion of the same figure. Therefore the apparent U-shaped form of the mass distribution is not direct evidence for two-body fission into pairs of charged fragments. The only direct evidence we find for such processes has already been discussed in connection with Fig. 8. We are, of course, unable to draw any conclusions regarding the mass distribution of the neutral fragments which accompany the ENHM fragments. A comparison of Fig. 12 with Fig. 3 in Ref. [18] (where the fragment detection efficiency was assumed to be 100%) shows that the calculated mass distribution is not very sensitive to the detection efficiency.

The coincidence data also demonstrate clearly that the lighter fragments shown in Fig. 12 are overwhelmingly generated in coincidence with other light (for the most part singly) charged fragments. This is especially evident from the contour shapes of the coincidence peaks as discussed in Sec. III. Few-body fragmentation events are relatively rare.

Nuclear multifragmentation displays features similar to those observed in our data on fullerene disintegration, e.g., the phenomenon of limiting fragmentation [52,53] (the fragmentation yield does not change much above a certain beam energy) that is reflected, for example, in the data shown in Fig. 4. Simply stated, the projectile can only deposit a limited amount of energy into the target. In proton-induced nuclear fragmentation, this limiting fragmentation is reached for beam energies greater than about 10 GeV and does not change much as the energy is raised up to 1 TeV. Another common feature is the U-shaped fragment-mass spectrum.

Both experiment (Fig. 12) and calculation display a power law falloff in the production cross sections for clusters of n carbon atoms, $\sigma(C_n)\propto n^{-\lambda}$, for $n\lesssim 20$. As indicated in Fig. 13 the experimental data give a value $\lambda\approx 1.3$, which is the same as the value derived from our calculation. This behavior is similar to the case of nuclear fragmentation (see, e.g., Ref. [52]), where one finds $\lambda\approx 2.6$ in inclusive (impact-parameter integrated) reactions. The power law is a consequence of the finiteness of the system and of the integration over different excitation energies in inclusive reactions [51].

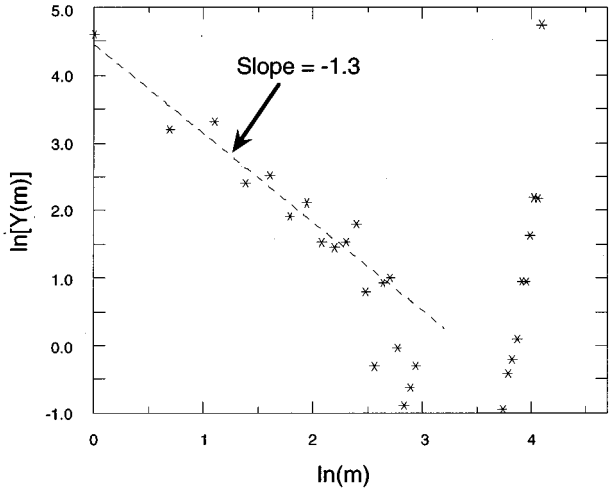

FIG. 13. A power-law fit to the low-mass part of the measured fragment-mass distribution (see text).

The nuclear fragmentation data contain indications of a second-order phase transition in nuclear matter (albeit washed out due to finite-size effects), and at the critical point the apparent exponent λ has a minimum [49–51]. Our λ value is significantly lower than the critical exponent ($\tau = 2.0$) for two-dimensional infinite-size bond percolation and can be attributed to the finiteness and the periodic boundary conditions of our fullerene. Similar observations [54] have been recorded for nuclear systems.

This opens an interesting avenue for further investigation of the disintegration of fullerenes, namely, the possibility of observing the remnants of a phase transition in a finite-size two-dimensional object with periodic boundary conditions. Finite-size effects could be studied with other heavier fullerenes, such as C_{70} and may lead to a better understanding of the finite-size scaling of critical phenomena.

The present calculations do not reproduce the observed odd-even effect in the production cross sections for small n. This effect can be understood in terms of the binding energies of small carbon clusters. Calculations [55] show that C_2 is bound by ≈ 3.1 eV/n and C_3 by ≈ 5.5 eV/n, and that in general [25,26] the binding of small linear chains with $2n$ members is weaker than those with $2n \pm 1$. The binding energy of a fragment, $E_b(n)$, enters into the final-state population via a factor $\exp(-[E^* - E_b]/T)$, where E^* is the mean excitation energy per carbon atom deposited in the fullerene, and T is the temperature of the fullerene at emission time. This explains qualitatively the odd-even effect in the observed cluster yields. Again, there is a parallel with nuclear fragmentation, for which the binding energies of the fragments have similar effects on the observed fragment-mass distributions [56]. For cluster sizes above $n \approx 10$, we observe intensity oscillations with period four, which we attribute to similar variations in the binding energies of carbon rings [25,26,55].

V. CONCLUSIONS

We have measured the relative yields for production of cluster fragments from the disintegration of C_{60} bombarded with high-energy, highly charged ions. We can explain the observed abundances by comparing the data to model calculations for the excitation of the giant plasmon and for multifragmentation in small-impact parameter collisions. The data show features similar to those seen in nuclear fragmentation. We expect that further studies will lead to a better understanding of the disintegration of small systems and possible extreme finite-size remnants of a phase transition.

ACKNOWLEDGMENTS

This work was supported by the U.S. Department of Energy, Office of Basic Energy Sciences, under Contract No. W-31-109-ENG-38. One of us (W.B.) acknowledges support from NSF. We thank Dr. K. R. Lykke for valuable conversations and we gratefully acknowledge the technical help of B. J. Zabransky and C. A. Kurtz and during the initial phases of this work, of M. A. Talebian and K. M. Teh.

[1] H. W. Kroto, J. R. Heath, S. C. O'Brien, R. F. Curl, and R. E. Smalley, Nature, **318**, 162 (1985).
[2] W. Krätschmer, L. D. Lamb, K. Fostiropoulos, and D. R. Huffman, Nature, **347**, 354 (1990).
[3] D. R. Huffman, Phys. Today **44** (11), 22 (1991).
[4] S. Della-Negra, A. Brunelle, Y. Le Beyec, J. M. Curaudeau, J. P. Mouffron, B. Waast, P. Håkansson, B. U. R. Sundqvist, and E. Parilis, Nucl. Instrum. Methods **B 74**, 453 (1993).
[5] See, for example, R. J. Doyle, Jr. and M. M. Ross, J. Phys. Chem. **95**, 4954 (1991).
[6] E. E. B. Campbell, A. Hielscher, R. Ehlich, V. Schyja, and I. V. Hertel, *Nuclear Physics Concepts in the Study of Atomic Cluster Physics* (Springer-Verlag, Berlin, 1992).
[7] See, for example, the following review articles: S. W. McElvany and M. M. Ross, J. Am. Soc. Mass Spectrom. **3**, 268, (1992). D. M. Gruen, Nucl. Instrum. Methods **B78**, 118 (1993). C. Lifschitz, Mass Spectrom. Rev. **12**, 262 (1993). E. E. B. Campbell *et al.* in *The Physics of Electronic and Atomic Collisions: XVIII International Conference*, edited by T. Andersen *et al.*, AIP Conf. Proc. No. 295 (AIP, New York, 1993), p. 697
[8] E. A. Rohlfing, D. M. Cox, and A. J. Kaldor, J. Chem. Phys. **81**, 3322 (1984).
[9] See, for example, P. Wurz and K. R. Lykke, J. Phys. Chem. **96**, 10 129 (1992).
[10] T. Weiske, D. K. Böhme, J. Hrusak, W. Krätschmer, and H. Schwarz, Angew. Chem. Int. Ed. Engl. **30**, 884 (1991).
[11] D. R. Luffer and K. H. Schram, Rapid Commun. Mass Spectrom. **4**, 552 (1992).
[12] P. Hvelplund, L. H. Andersen, H. K. Haugen, J. Lindhard, D. C. Lorents, R. Malhotra, and R. Ruoff, Phys. Rev. Lett. **69**, 1915 (1992).
[13] H. Hohmann, C. Callegari, S. Furrer, D. Grosenick, E. E. B. Campbell, and I. V. Hertel, Phys. Rev. Lett. **73**, 1919 (1994).
[14] K. R. Lykke, Phys. Rev. A **52**, 1354 (1995).
[15] J. Jin, H. Khemliche, M. H. Prior, and Z. Xie Phys. Rev. A **53**, 615 (1996).
[16] P. Scheier, B. Dünser, and T. D. Märk, Phys. Rev. Lett. **74**, 3368 (1995).
[17] B. Walch, C. L. Cocke, R. Völpel, and E. Salzborn, in *VIth International Conference on the Physics of Highly Charged Ions*, edited by P. Richard *et al.*, AIP Conf. Proc. No. 274 (AIP, New York, 1993), p. 602; Phys. Rev. Lett. **72**, 1439 (1994).
[18] T. LeBrun, H. G. Berry, S. Cheng, R. W. Dunford, H. Esbensen, D. S. Gemmell, and E. P. Kanter, Phys. Rev. Lett. **72**, 3965 (1994).
[19] Purchased from MER Corporation, Tucson, AZ.
[20] R. W. Dunford, C. J. Liu, N. B. Mansour, Y. Azuma, H. G. Berry, D. A. Church, T. P. Dinneen, L. Young, and B. J. Zabransky, Nucl. Instrum. Methods B **43**, 459 (1989).
[21] A. Tokmakoff, D. R. Haynes, and S. M. George, Chem. Phys. Lett. **186**, 450 (1991).
[22] See, for example, R. Meir and P. Eberhardt, Int. J. Mass Spec-

trom. Ion Process. **123**, 19 (1993).
[23] R. Völpel, G. Hofmann, M. Steidl, M. Stenke, M. Schlapp, R. Trassl, and E. Salzborn, Phys. Rev. Lett. **71**, 3439 (1993).
[24] J. H. D. Eland, Mol. Phys. **61**, 725 (1987).
[25] Von E. Dörnenburg and H. Hintenberger, Z. Naturforsch. **14A**, 765 (1959).
[26] G. von Helden, M-T. Hsu, N. Gotts, and M. T. Bowers, J. Phys. Chem. **97**, 8182 (1993).
[27] J. H. D. Eland, Int. J. Mass Spectrom. Ion Phys. **8**, 143 (1972).
[28] J. H. D. Eland, Int. J. Mass Spectrom. Ion Phys. **8**, 153 (1972).
[29] G. F. Bertsch, A. Bulgac, D. Tomanek, and Y. Wang, Phys. Rev. Lett. **67**, 2690 (1991).
[30] I. V. Hertel, H. Steger, J. de Vries, B. Weisser, C. Menzel, B. Kamke, and W. Kamke, Phys. Rev. Lett. **68**, 784 (1992).
[31] J. W. Keller and M. A. Coplan, Chem. Phys. Lett. **193**, 89 (1992).
[32] B. Wästberg and G. Wendin, Nucl. Instrum. Methods B **87**, 162 (1994).
[33] P. W. Fowler, P. Lazzeretti, and R. Zanasi, Chem. Phys. Lett. **165**, 79 (1990).
[34] N. Van Giai and E. Lipparini, Z. Phys. D **27**, 193 (1993).
[35] D. Östling, P. Apell, and A. Rosén, Europhys. Lett. **21**, 539 (1993).
[36] K. Yabana and G. F. Bertsch, Phys. Sci. **48**, 633 (1993).
[37] G. Barton and C. Eberlein, J. Chem. Phys. **95**, 1512 (1991).
[38] M. Ya. Amusia and A. V. Korol, Phys. Lett. A **186**, 230 (1994).
[39] G. Gensterblum *et al.*, Phys. Rev. Lett. **67**, 2171 (1991).
[40] R. K. Yoo, B. Ruscic, and J. Berkowitz, J. Chem. Phys. **96**, 911 (1992).
[41] N. Bohr, K. Dan. Vidensk. Selsk. Mat. Fys. Medd. **18** (8), 1 (1948).
[42] A. S. Schlachter, J. W. Stearns, W. G. Graham, K. H. Berkner, R. V. Pyle, and J. A. Tanis, Phys. Rev. A **27**, 3372 (1983).
[43] J. D. Jackson, *Classical Electrodynamics* (Wiley, New York, 1962).
[44] See, for example, E. Merzbacher, Quantum Mechanics (Wiley, New York, 1970), p. 367.
[45] R. Schmidt *et al.*, Phys. Rev. Lett. **70**, 1767 (1993).
[46] H. Emling, Prog. Part. Nucl. Phys. **33**, 729 (1994).
[47] T. Drewello, W. Krätschmer, M. Fieber-Erdman, and A. Ding, Int. J. Mass Spectrom. Ion Process. **124**, R1 (1993).
[48] T. L. Ferrell and P. M. Echenique, Phys. Rev. Lett. **55**, 1526 (1985).
[49] W. Bauer, D. R. Dean, U. Mosel, and U. Post, Phys. Lett. B **150**, 53 (1985).
[50] W. Bauer, U. Post, D. R. Dean, and U. Mosel, Nucl. Phys. A **452**, 699 (1986).
[51] W. Bauer, Phys. Rev. C **38**, 1297 (1988).
[52] A. Hirsch *et al.*, Phys. Rev. C **29**, 508 (1984).
[53] G. Rudstam, Z. Naturforsch. **21A**, 1027 (1966).
[54] L. Phair, W. Bauer, and C. K. Gelbke, Phys. Lett. B **314**, 271 (1993).
[55] D. Tomanek and M. A. Schluter, Phys. Rev. Lett. **67**, 2331 (1991).
[56] D. J. Fields, C. K. Gelbke, W. G. Lynch, and J. Pochodzalla, Phys. Lett. B **187**, 257 (1987).